SUPPORTING INFORMATION

Origin of Photovoltaic Losses in Selenium Solar Cells with Open-Circuit Voltages Approaching 1 V

Rasmus Nielsen[1,*], Tomas H. Youngman[1], Hadeel Moustafa[2], Sergiu Levcenco[3], Hannes Hempel[3], Andrea Crovetto[3], Thomas Olsen[2], Ole Hansen[4], Ib Chorkendorff[1], Thomas Unold[2], and Peter C. K. Vesborg[1]

[1]SurfCat, DTU Physics, Technical University of Denmark, DK-2800 Kgs. Lyngby, Denmark
[2]CAMD, DTU Physics, Technical University of Denmark, DK-2800 Kgs. Lyngby, Denmark
[3]Department of Structure and Dynamics of Energy Materials, Helmholtz-Zentrum Berlin für Materialien und Energie GmbH, Berlin, Germany
[4]DTU Nanolab, National Center for Nano Fabrication and Characterization, Technical University of Denmark, DK-2800, Kgs. Lyngby, Denmark
[*]E-mail: raniel@dtu.dk

Conductivity mass tensor

The symmetry of trigonal selenium requires that second rank material tensors such as the conductivity tensor $\bar{\sigma}$ and thus also the inverse conductivity mass tensor $1 = \bar{m}$ have the topology

$$\bar{\sigma} = \begin{pmatrix} \sigma_\perp & 0 & 0 \\ 0 & \sigma_\perp & 0 \\ 0 & 0 & \sigma_\parallel \end{pmatrix}, \qquad \text{and} \qquad 1/\bar{m} = \begin{pmatrix} 1/m_\perp & 0 & 0 \\ 0 & 1/m_\perp & 0 \\ 0 & 0 & 1/m_\parallel \end{pmatrix}$$

in the natural coordinate system. [1]

Both the conduction and the valence band of trigonal selenium have several equivalent extrema in first Brillouin zone, as illustrated in Fig S1. The inverse mass tensor of these extrema may have less symmetry than the inverse conductivity mass tensor, but the symmetric arrangement of extrema ensures that the inverse conductivity mass tensor enjoys the full symmetry.

The conduction band minima are at high symmetry points and thus the inverse conductivity mass tensor elements derive directly from the band curvatures and we have $m_{c\perp} = 0.39 \times m_0$ and $m_{c\parallel} = 0.18 \times m_0$, where m_0 is the free electron mass.

The valence band is more complicated and the individual maxima far more anisotropic (also in the plane). Therefore, the conductivity mass tensor is calculated as the mean of rotated tensors for the individual maxima to arrive at $m_{v\perp} = 0.68 \times m_0$ and $m_{v\parallel} = 0.21 \times m_0$.

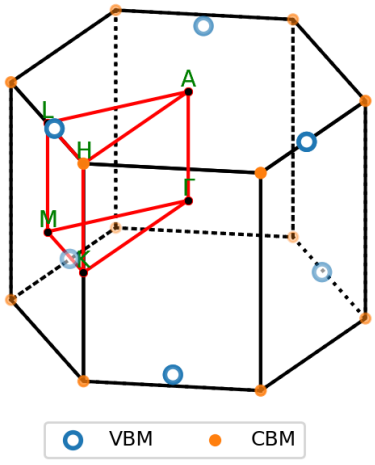

Figure S 1: Positions of the equivalent conduction band minima (CBM) and valence band maxima (VBM).

Additional figures

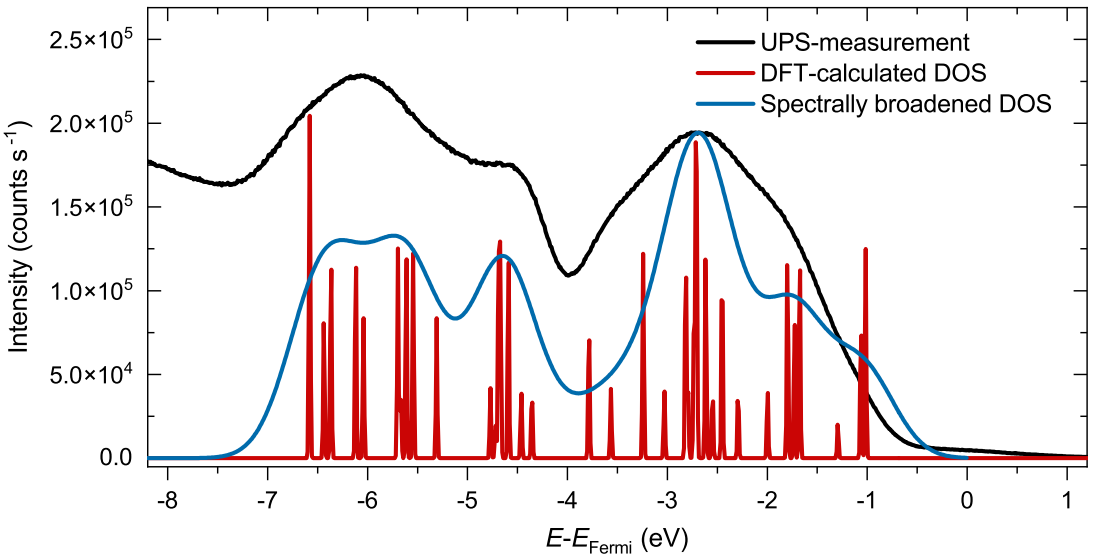

Figure S 2: Ultraviolet photoemission spectroscopy measurements of the valence band structure of poly-Se compared to first-principles calculations of pristine selenium with and without spectral broadening. The UPS-survey is carried out in a commercial Thermofisher Scientific Nexsa XPS system using a helium discharge lamp as a photon source with principal photon energies of 21.2 eV (He I) and 40.8 eV (He II). The sample surface is cleaned using a 30 s Ar^+-ion etching in a 4x4 mm raster. The binding energy scale is corrected by measuring the Fermi-edge of a surface cleaned Au-reference, and the Au-reference is in electrical contact with the selenium sample to ensure a common Fermi-level position in equilibrium. The pass energy is set to 2.0 eV, the dwell time is set to 50 ms, and the final spectrum is an average of 20 scans.

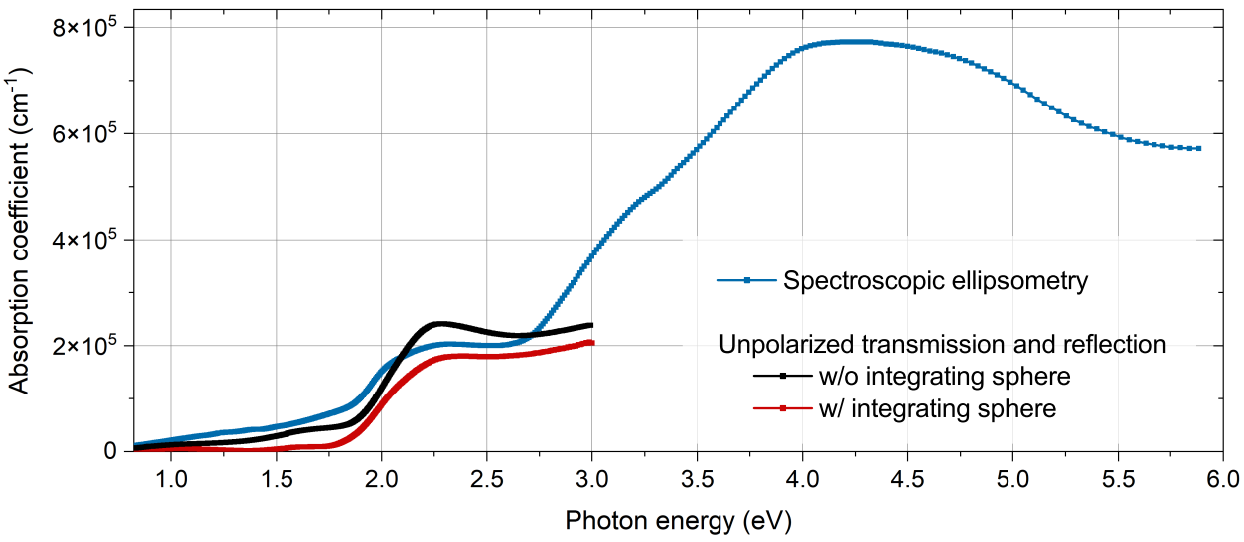

Figure S 3: Extended spectra of the derived absorption coefficient of poly-Se. The higher apparent absorption coefficient derived by the measurements that do not involve an integrating sphere is likely a result of light scattering effects.

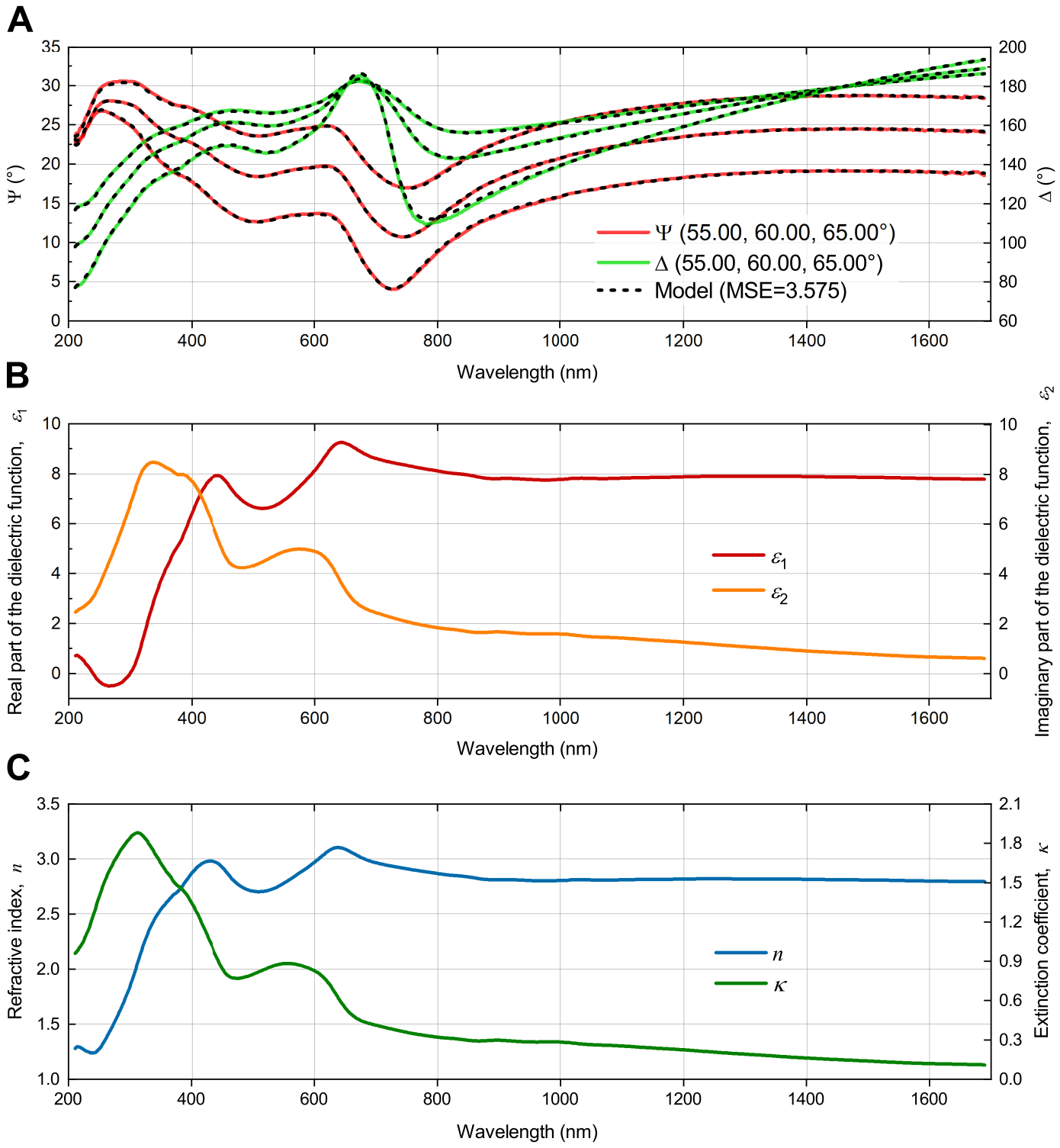

Figure S 4: Variable angle spectroscopic ellipsometry of ∼130 nm poly-Se synthesized on quartz. (**A**) The ratio of amplitude diminutions (Ψ), the phase shift (Δ), and the optical model fitted to the raw data with a mean square error of 3.575. (**B**) The imaginary part of the dielectric function is fitted to a B-spline function with 10 nodes/eV in the range 600-800 nm, and 5 nodes/eV elsewhere. The real part is derived from Kramers-Kronig integration. (**C**) From the dielectric function, the refractive index n and the extinction coefficient κ are derived using standard optical relations.

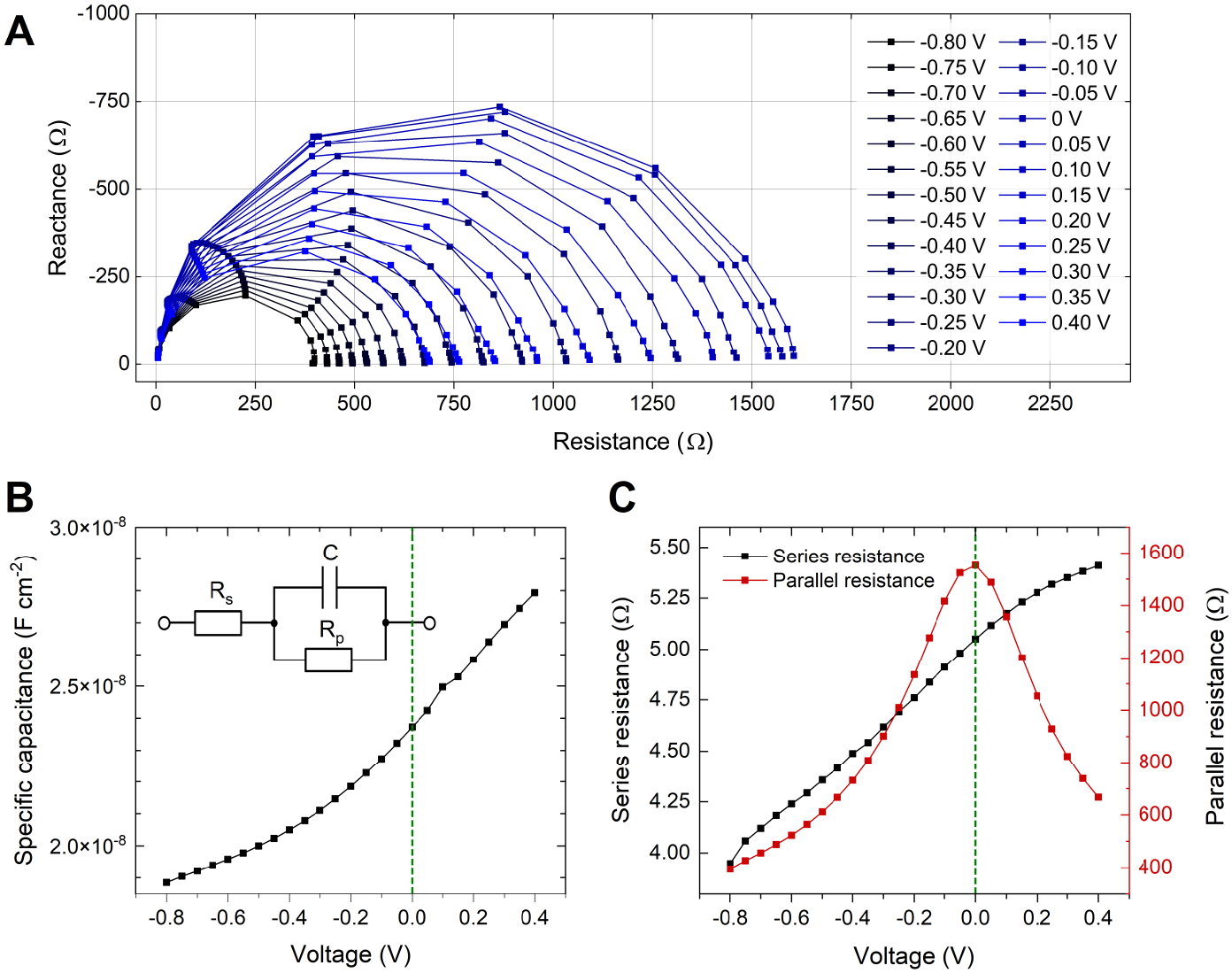

Figure S 5: Impedance spectroscopy measurements and results from numerical fitting of the entire frequency spectra to a Randles circuit. (**A**) Nyquist plot showing the frequency response of a complete solar cell at various applied DC biases. The pn-heterojunction of the device under test comprise TiO_2/Te/poly-Se. (**B**) The specific capacitance as a function of applied DC voltage normalized using the active area A = 0.37 cm^2 of the device under test. (**C**) Series and parallel resistances as a function of applied DC voltage. The internal series resistance of the device is expected to increase with increasing forward bias as the depletion region width decreases. The parallel conductance (i.e. the inverse of the parallel resistance) is expected to increase exponentially with applied forward bias in agreement with data. However, the parallel conductance due to generation of charge carriers in the depletion layer is expected to decrease with reverse bias, contrary to the data, which suggests a different origin for the majority carriers of the reverse current.

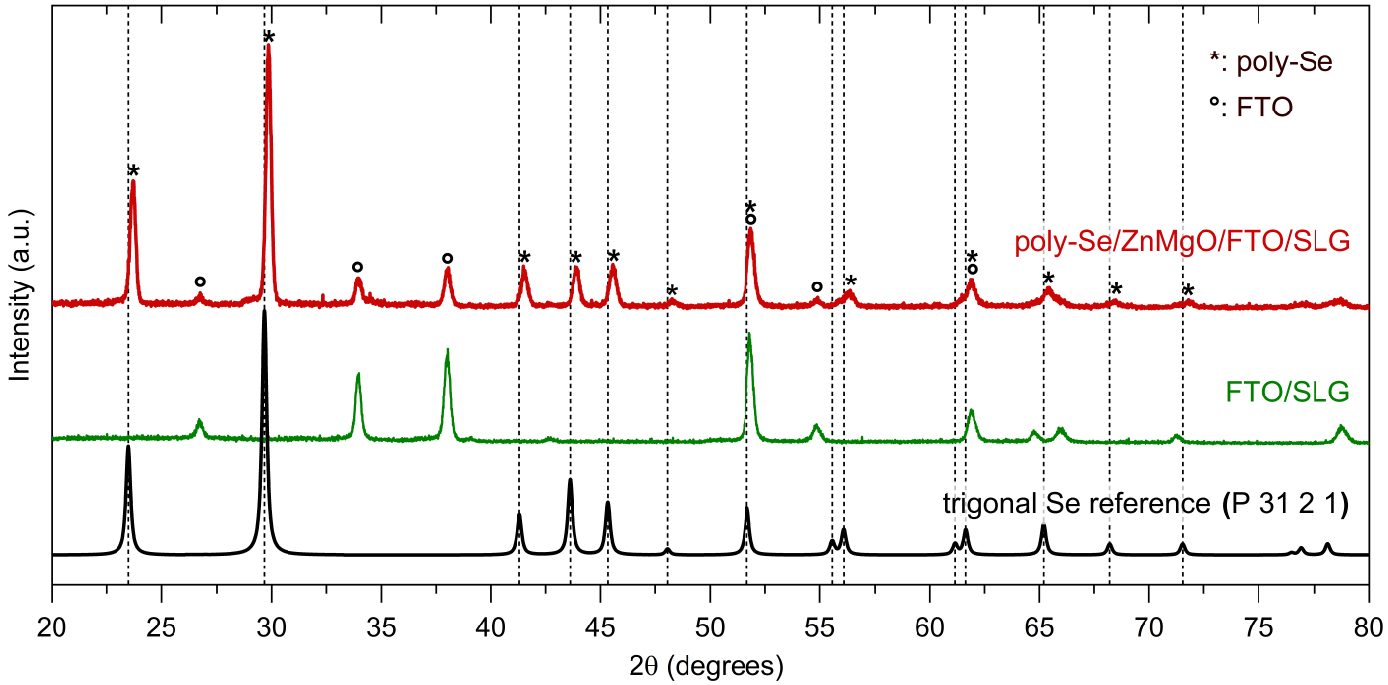

Figure S 6: Grazing incidence X-ray diffraction (GIXRD) patterns of poly-Se synthesized on ZnMgO. Bare FTO-coated glass substrates were measured as a reference before sputter depositing ZnMgO and synthesizing the poly-Se photoabsorber on top. All the observed Bragg peaks are either accounted for by the FTO-substrate or the trigonal selenium reference (collection code 40018 in the Inorganic Crystal Structure Database, ICSD). The measurements are carried out in a Panalaytical Empyrean XRD using a parallel plate collimator at an angle of 0.5°. The source was a Cu LFF HR gun operated at 45 kV and 40 mA, with $K_{\alpha 1} = 1.540598$ Å.

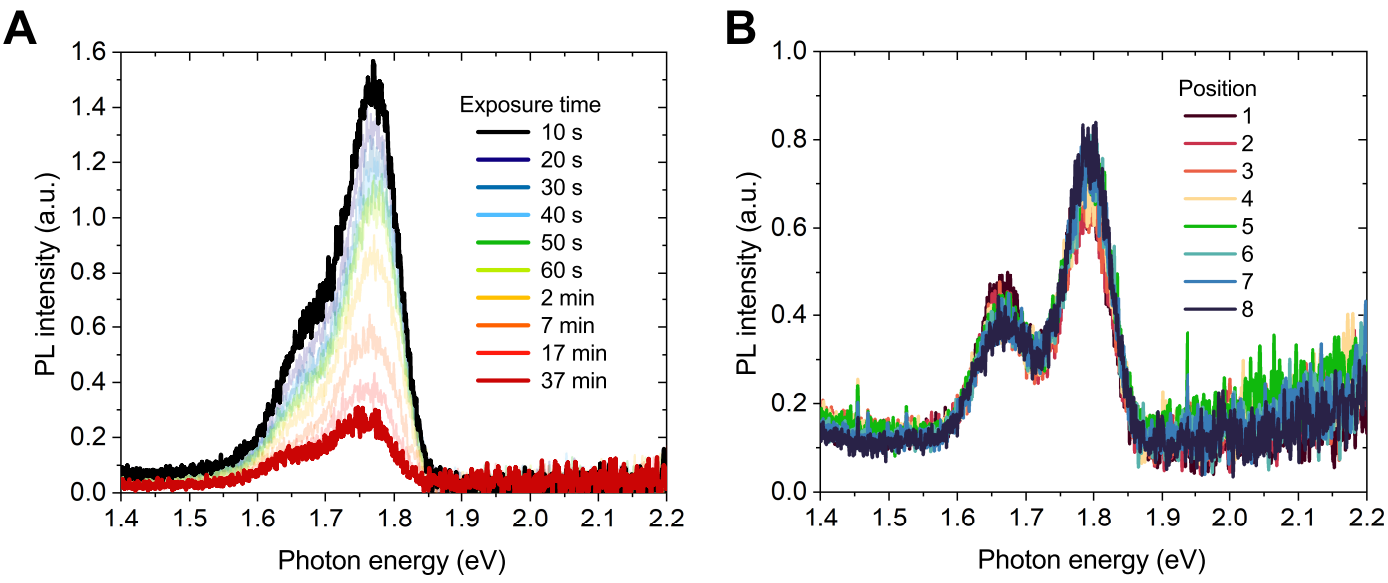

Figure S 7: Photoluminescence (PL) degradation effects in poly-Se on quartz at T = 15 K. (**A**) Irreversible attenuation of the PL intensity as a function of exposure time. The exact origin of the observed degradation effect is still unclear. (**B**) PL spectra obtained from scanning the laser beam spot to 8 unexposed positions on the sample surface ∼1 mm apart, each new position is exposed a total of 10 seconds. The overlap of the 8 spectra is indicative of a great spatial homogeneity. As the PL signal is constant when scanning the laser, this approach is used to record the temperature dependent PL spectra in Fig 4. All photoluminescence measurements are carried out using a 532 nm laser with a spot diameter of 100 μm and an optical power density $P_{\text{opt}} = 3.7\,\text{W}\,\text{cm}^{-2}$ on the sample surface.

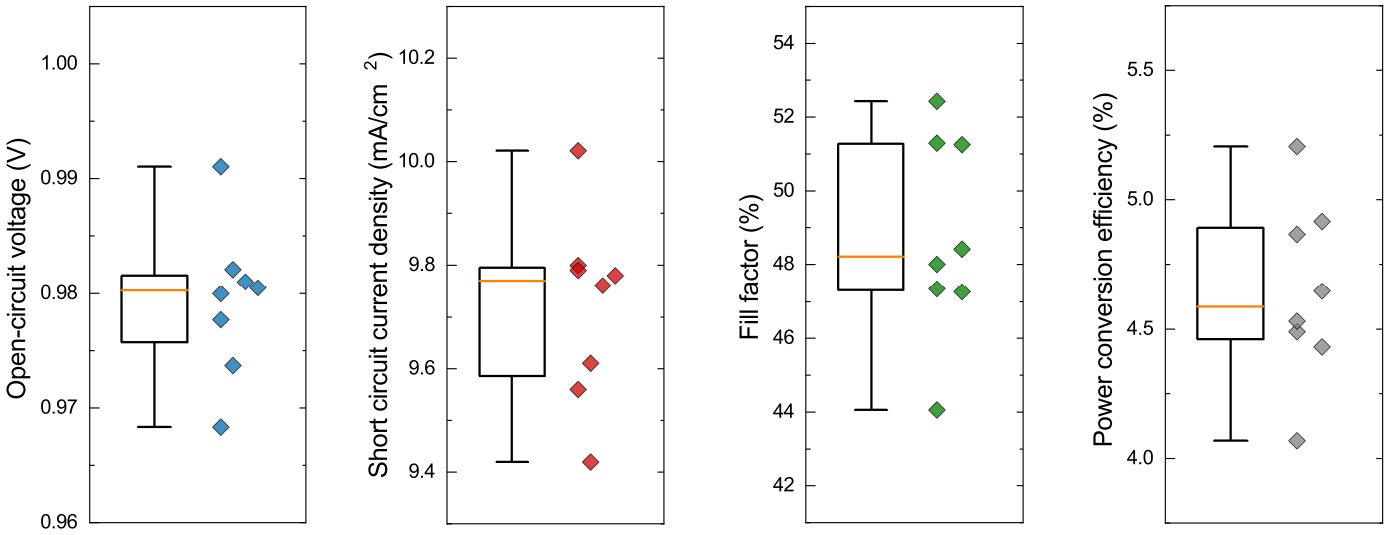

Figure S 8: Statistical performance data for a single batch of devices with an active cell area of 0.30 cm^2.

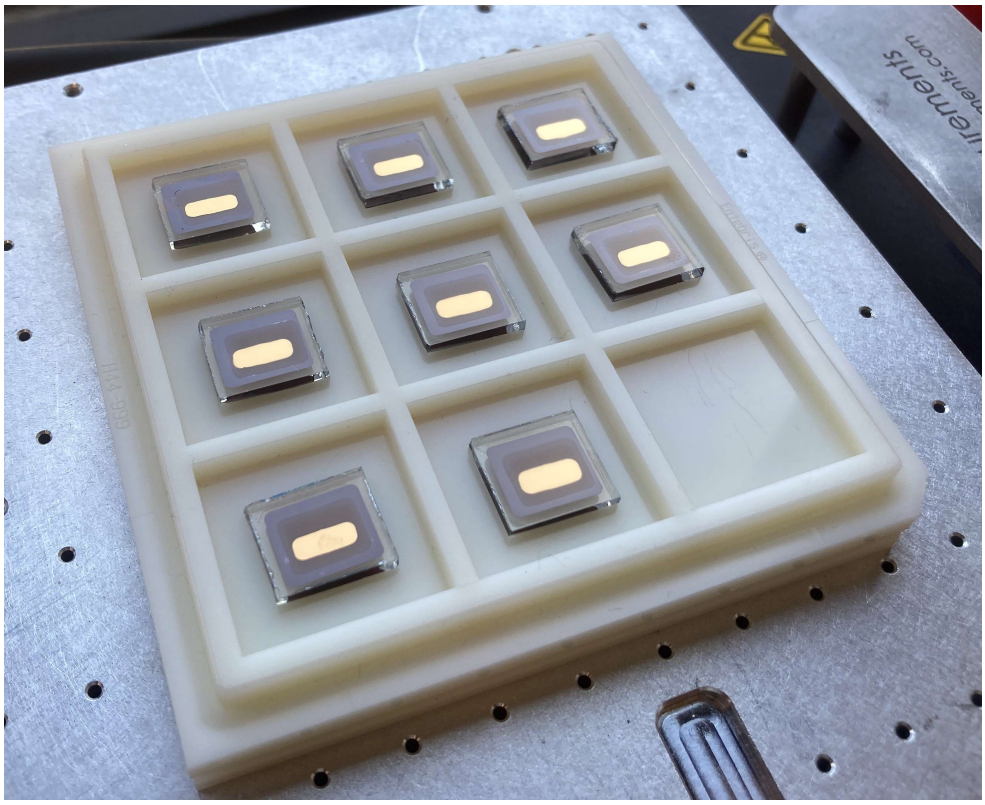

Figure S 9: Visual appearance of all parallel-processed devices in a single batch.

References

[1] R. E. Newnham, *Properties of Materials: Anisotropy, Symmetry and Structure*, Oxford University Press Inc., 2005.